Article

Isothermal solidification for high-entropy alloy synthesis

https://doi.org/10.1038/s41586-025-09530-w

Received: 13 December 2024

Accepted: 13 August 2025

Published online: 24 September 2025

Check for updates

Qiubo Zhang[1,2], Max C. Gallant[1,2], Yi Chen[1,2], Zhigang Song[1], Yang Liu[3], Qi Zheng[1], Linfeng Chen[4], Karen. C. Bustillo[5], Yu Huang[3], Kristin A. Persson[1,2] & Haimei Zheng[1,2]✉

Kinetically trapping the high-temperature states through rapid cooling solidification is widely used for the synthesis of high-entropy alloys (HEAs), especially those with intrinsically immiscible elemental combinations[1–4]. However, strategies need to be developed to overcome the fundamental limitations of rapid cooling solidification in controlling the crystallinity, structure and morphology of HEAs. Here we introduce an isothermal solidification strategy for the synthesis of HEAs by rapidly altering the metal alloy composition through liquid–liquid interface reactions at low temperatures, for example, from 25 °C to 80 °C. We use gallium (Ga)-based metal as the sacrificial reagent and mixing medium. By directing the reactions to the interfaces between the Ga-based liquid metal and an aqueous metal ion solution, the foreign metal ions can be reduced at the interfaces and incorporated into the liquid metal quickly. HEAs with various crystallinity (single crystal, mesocrystal, polycrystal and amorphous), morphology (zero, two and three dimensions) and compositions can be achieved through the isothermal solidification. Ga can be completely consumed, resulting in Ga-free HEAs. If desired, Ga can be one of the metal elements in the final products. In situ liquid phase transmission electron microscopy (TEM) studies and theoretical analysis show the isothermal solidification mechanisms. Our direct observations show the enhanced mixing of liquid metal elements and the solidification process with fluctuating nucleation dynamics. The isothermal solidification marks a powerful strategy for HEA synthesis through an unexplored pathway of kinetically trapping the high-entropy states.

High-entropy alloy (HEA) nanomaterials have attracted marked interest because of their prospective applications in catalysis[1,5–9], batteries[10] and others[11]. For the intrinsically immiscible metal element combinations under thermodynamic equilibrium, using the method of rapid cooling from the high-temperature states (for example, above 2,000 K) is effective for trapping the high-entropy states to obtain HEAs[1–4,12]. Synthesis of these HEAs by rapid cooling solidification predominantly yields nanoparticles with little control over their structure and morphology[2,6,8]. Wet-chemical approaches provide versatility in lower-temperature synthesis of HEAs with various particle sizes, morphology and structure[2,13–15], but they are mainly applicable to combinations of miscible elements in near equilibrium thermodynamic processes. To date, innovative approaches remain to be explored to overcome the limitations imposed by these techniques.

In this work, we introduce an isothermal solidification strategy for the synthesis of HEAs at low temperature. By directing the metal ion reduction reactions to the interfaces between the Ga or Ga-based liquid metal and an aqueous salt solution, the formation of HEAs with control of crystallinity, morphology and structure is realized, including those with intrinsically immiscible metal element combinations. We monitor the dynamic solidification processes at the atomic level using state-of-the-art liquid-cell TEM technology to reveal the underlying mechanisms. The isothermal solidification of HEAs marks a breakthrough in HEA synthesis, providing a viable alternative to rapid cooling for trapping the liquid alloy states.

Principles of isothermal solidification

Figure 1a shows the fundamental principle of the isothermal solidification strategy for HEAs synthesis, in which the high-entropy states are achieved through rapid composition changes under a constant temperature. The formation of HEAs involves two steps. In step I, the metal ions from the salt solution are reduced by Ga at the interfaces between the liquid metal and the salt solution (liquid–liquid interface). The reduction reaction is restricted to the liquid–liquid interface because of the nature of the reaction ($Ga + \frac{3}{x}M^{x+} \rightarrow Ga^{3+} + \frac{3}{x}M$, where Ga is from the liquid metal, M is the foreign metal from the salt solution, and x represents the valence state). In step II, the generated foreign metal atoms readily dissolve into the liquid metal. As Ga-based liquid metals (for example, Ga or Ga-based alloys; Extended Data Figs. 1 and 2 and

[1]Materials Sciences Division, Lawrence Berkeley National Laboratory, Berkeley, CA, USA. [2]Department of Materials Science and Engineering, University of California, Berkeley, Berkeley, CA, USA. [3]Department of Materials Science and Engineering, University of California, Los Angeles, Los Angeles, CA, USA. [4]Inorganic Nanostructures, Molecular Foundry, Lawrence Berkeley National Laboratory, Berkeley, CA, USA. [5]National Center for Electron Microscopy, Molecular Foundry, Lawrence Berkeley National Laboratory, Berkeley, CA, USA. ✉e-mail: hmzheng@lbl.gov

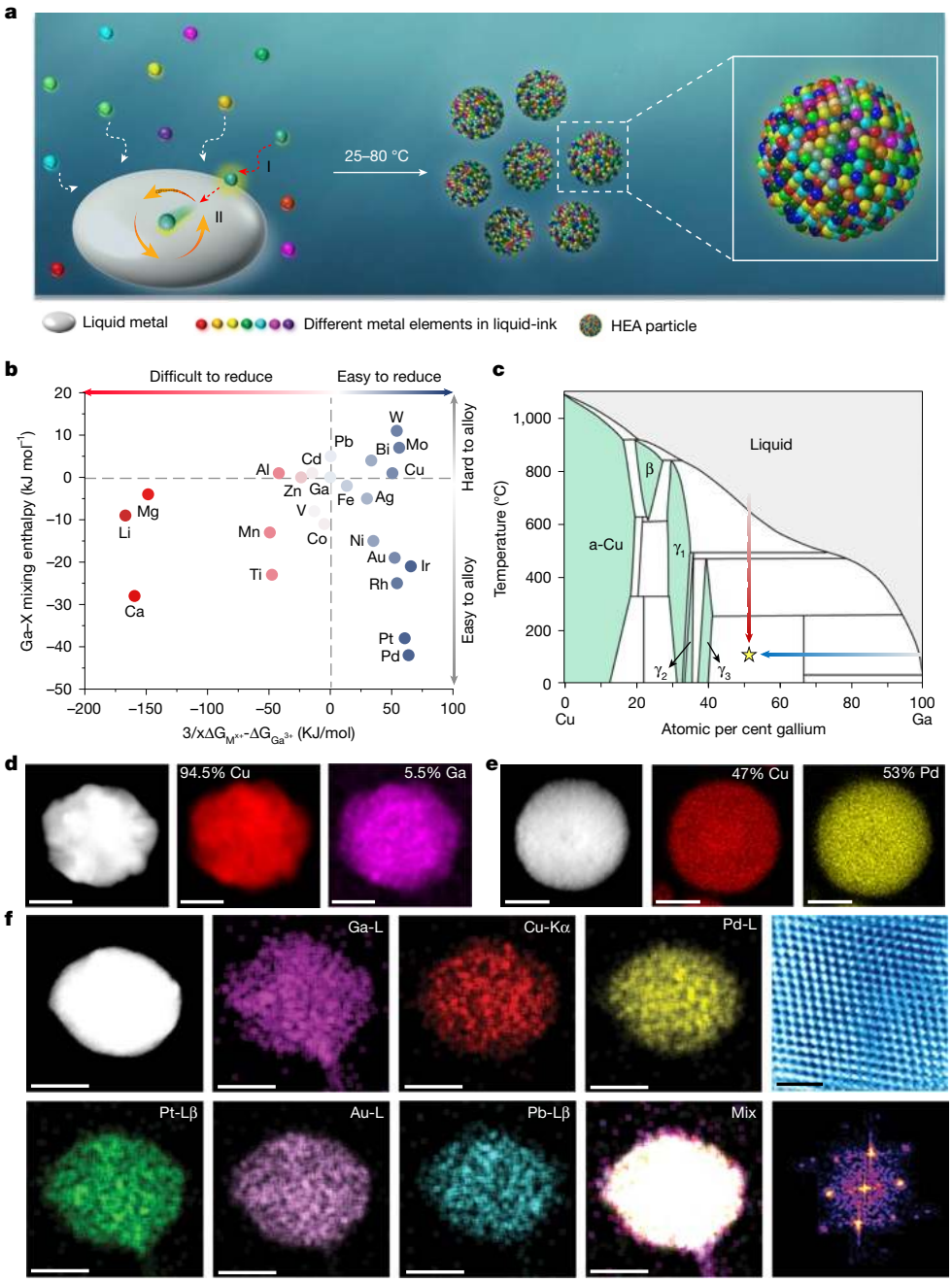

Fig. 1 | Fundamental principles of isothermal solidification synthesis of HEAs at low temperatures. a, Schematic of HEA synthesis by isothermal solidification achieved through liquid–liquid interface reactions. The synthesis process consists of two steps: (step I) reduction of foreign metal ions at the interface between the liquid metal and liquid salt solution; and (step II) incorporation of metal atoms from step I into the liquid metal and isothermal solidification to form HEAs. **b**, Thermodynamically informed design map. The reducibility ($\frac{3}{x}\Delta G_M^{x+} - \Delta G_{Ga}^{3+}$) of metals is considered to assess the feasibility of the reduction reaction in step I. Metals corresponding to ions positioned to the right of the dashed line can be spontaneously reduced by Ga at room temperature. The mixing enthalpy between Ga and other metals serves as an indicator of alloy miscibility in step II. It is noted that we list only the mixing enthalpy of binary alloys here (the values of binary liquid alloys were calculated using the Miedema model at an equiatomic composition)[22]. For multi-element alloys, the miscibility is governed by the mixing entropy of the entire element system. **c**, Phase diagram of a representative Cu–Ga binary alloy, demonstrating two solidification routes. The rapid cooling solidification may kinetically trap the high-temperature states to form HEAs (indicated by the red arrow). For isothermal solidification, the high-entropy states of liquid alloy can be trapped by rapidly changing the composition at low temperatures (as highlighted by the blue arrow). **d**, Scanning TEM (STEM) and EDS elemental mapping of a representative Ga–Cu alloy. **e**, STEM–EDS elemental mapping of a representative Pd–Cu alloy. **f**, STEM–EDS elemental maps, HRTEM image and fast Fourier transform (FFT) pattern of an individual HEA-NP, showing the formation of a solid-solution structure by isothermal solidification synthesis at 60 °C. Scale bars, 100 nm (**d**,**e**); 10 nm (**f**, EDX maps); 1 nm (**f**, HRTEM image).

Supplementary Fig. 1) interact strongly with other metal elements, they are ideal solvents for the dynamic mixing of metal elements[12,16,17]. The liquid–liquid interface reaction facilitates the rapid incorporation of newly formed metal atoms into the liquid metal alloy; thus, the reaction is continuously refreshed, and an accelerated composition increase of the liquid metal alloy can be achieved because of the spontaneous, rapid incorporation of foreign metal atoms as well as the consumption of Ga metal in the liquid metal[18,19]. The abrupt composition change leads

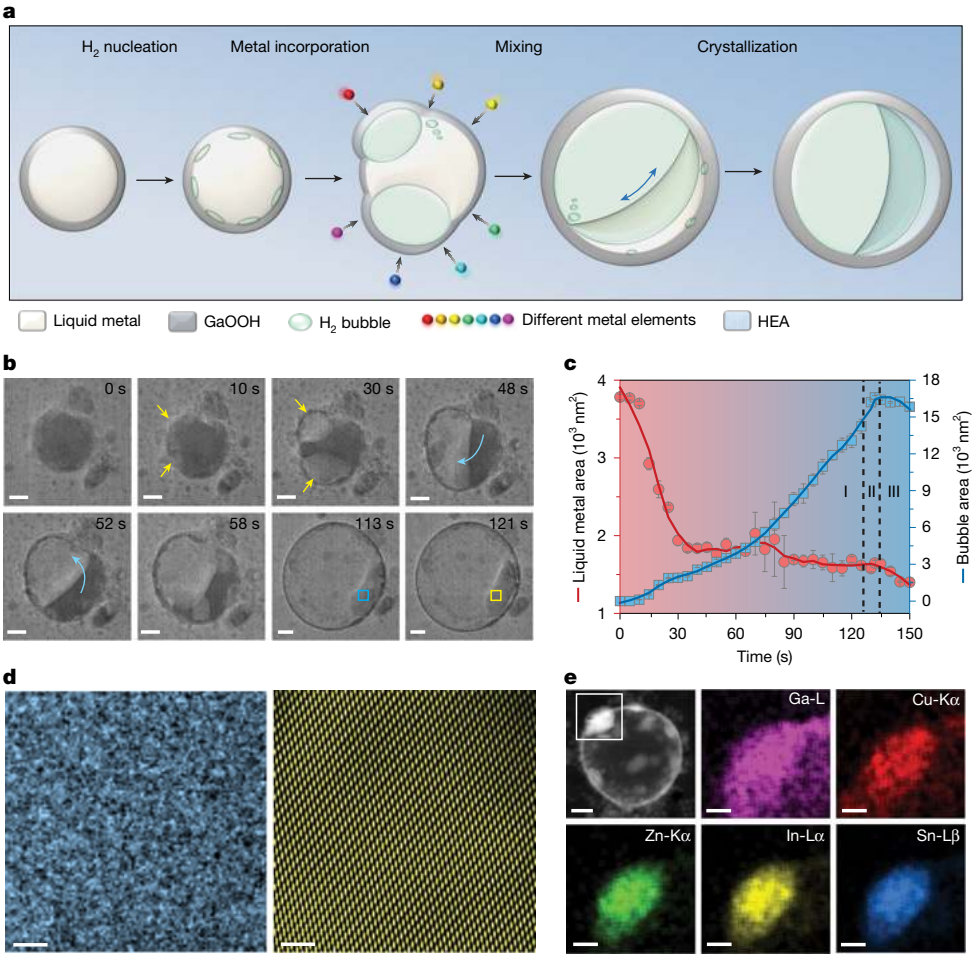

Fig. 2 | Mechanisms of isothermal solidification for the formation of HEA-NPs shown through in situ liquid-phase TEM at 60 °C. a, Schematic of the formation of HEA-NPs, showing the steps of H_2 nucleation, metal incorporation, incorporation of metal elements and crystallization. **b**, Sequential in situ TEM images capture the formation of a HEA-NP (GaInSnZnCu) within a liquid environment at 60 °C. Yellow arrows highlight H_2 bubble nucleation and growth, whereas the blue arrow indicates the stirring direction of the liquid metal alloy. **c**, Projected areas of the metal alloy and bubbles over time. Intervals I, II and III represent stages in the dynamic process. Data are presented as mean ± standard deviation, based on three independent measurements ($n = 3$), with error bars representing standard deviation. **d**, HRTEM images show structural features of the same area before and after solidification of the liquid metal alloy, corresponding to the blue and yellow squares in **b**. **e**, STEM–EDS mapping shows the elemental distribution within the synthesized HEA-NP. Scale bars, 2 nm (**d**); 50 nm (**e**, extreme left top); 20 nm (**b**,**e**, second from left to remaining).

to the liquid metal alloy entering a supercooled state, triggering isothermal solidification to kinetically trap the high-entropy states. For the synthesis of HEAs using Ga liquid metal, the reducibility and miscibility of metals are governed by two parameters[20,21] (Fig. 1b): the reducibility of metal ions by Ga is estimated by $\frac{3}{x}\Delta G_M^{x+} - \Delta G_{Ga}^{3+}$, which accounts for the feasibility of the reduction reaction in step I. The miscibility of metals with Ga is represented by the mixing enthalpy (ΔH_{mix}), which describes the readiness of the foreign metal to alloy with Ga in step II. The ΔH_{mix} values were calculated based on Miedema's model for equimolar (1:1) solid-state mixtures of Ga–X pairs at room temperature[22]. Because the product composition varies during isothermal solidification and the mixing process occurs in the liquid state, we treat these ΔH_{mix} values as a qualitative indicator for the tendency to form a solid solution in step II based on phase formation rules[23,24]. According to these criteria, elements positioned in the first and fourth quadrants of Fig. 1b correspond to those that can undergo spontaneous reduction from their aqueous metal chloride solutions. Moreover, elements positioned near the left of the vertical boundary (for example, Cd, V and Co) can also undergo reduction on thermal heating.

We exemplify this isothermal solidification strategy using the Ga–Cu binary alloy[24], which features a low solubility of Cu in liquid Cu–Ga alloy at temperatures below 100 °C (less than 3%). The widely used rapid cooling solidification of the high temperature Ga–Cu liquid alloys leads to kinetically trapping of the alloy mixture, as highlighted by the red arrow (Fig. 1c). However, as an alternative route highlighted by the blue arrow, greatly increasing the miscibility of Cu in liquid Ga creates an oversaturated liquid alloy (a supercooled liquid state) and the subsequent isothermal solidification yields a high-Cu-content alloy.

We synthesized binary Cu–Ga alloys using the isothermal solidification method at a constant temperature of 60 °C. Energy-dispersive X-ray spectroscopy (EDS) analysis (Fig. 1d) shows that the Cu content reached up to 95%, with the two elements homogeneously distributed. Moreover, the isothermal solidification may also generate Ga-free alloys, for example, Cu–Pd alloys are achieved (Fig. 1e). The isothermal solidification can effectively synthesize HEAs with arbitrary elemental compositions (Fig. 1f, Supplementary Fig. 2 and Supplementary Table 1).

In situ TEM dynamics

To uncover the underlying mechanisms of isothermal solidification for HEAs synthesis, we conduct direct observation of the alloying process at the atomic level using advanced liquid cell TEM (Figs. 2 and 3

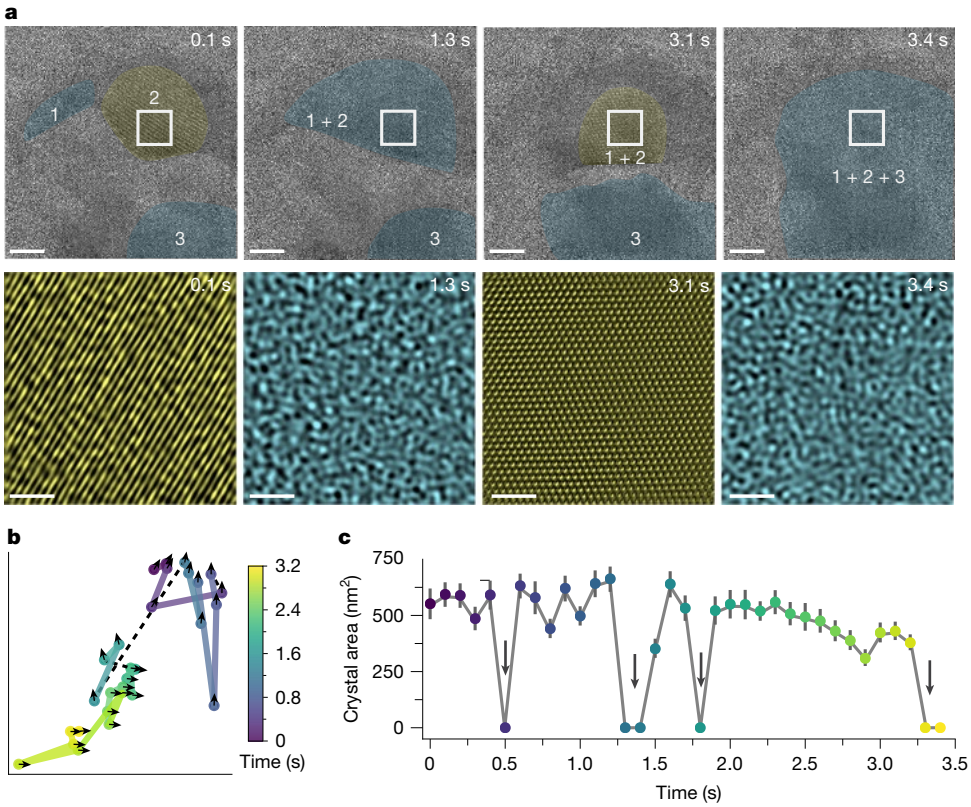

Fig. 3 | Structural fluctuations during the alloying and crystallization process. a, Sequential images (top row) and the corresponding HRTEM images of the highlighted white square area (bottom row) show the fluctuations of crystal structure, projected area and shape of the crystal domain during alloying and crystallization process. Blue colour highlights the amorphous structure, whereas the yellow colour indicates the crystalline region. **b**, Trajectory of the centre of the highlighted crystalline region during alloying. Arrows indicate the lattice orientation. **c**, Changes of the crystalline region over time. Arrows point out the moments with complete amorphization. Scale bars, 10 nm (**a**, top row); 2 nm (**a**, bottom row).

and Supplementary Videos 1 and 2). In a simplified model system, we introduce Cu as a single additional element into the host liquid metal of Ga-based alloy (for example, GISZ, composed of Ga, In, Sn and Zn) to form single-crystal high-entropy alloy nanoparticles (HEA-NPs), specified as GaSnInZnCu.

We track the dynamic evolution of the HEA-NPs formation. At the initial stage (Fig. 2a), the liquid metal nanoparticle is encased in a Ga_2O_3 shell (Extended Data Fig. 1), which transforms into GaOOH through a hydrolysis reaction in the aqueous solution[25]. Ga from the liquid metal reacts with cations in the solution (for example, H^+ and Cu^{2+}), generating H_2 gas and Cu metal atoms. The formation of H_2 is marked by the appearance of nanobubbles at the GaOOH–liquid metal interface (Fig. 2b, yellow arrows). The generated Cu atoms are incorporated into the liquid metal, as evidenced by EDS characterization of the final HEA (Fig. 2e). Small gas bubbles coalesce into a larger bubble while the liquid metal circulates along the inner shell (indicated by blue arrows) (30–58 s). This hydrogen-gas-assisted stirring greatly enhances the metal element mixing (Supplementary Video 3 and Supplementary Figs. 3 and 4). As the reaction proceeds, gas bubbles continue to evolve, driving the bubble expansion (Fig. 2a–c). Simultaneously, Ga is gradually depleted from the liquid metal, whereas Cu atoms continuously join in (Fig. 2c). After 121 s, the fluidity of the liquid metal alloy quickly decreases, signalling its transition to a solid state (Fig. 2d). The temperature remains at 60 °C throughout the alloying and solidification processes, indicating the isothermal solidification. During the final crystallization, the gas bubble briefly expands before contracting, and the liquid metal undergoes slight reshaping before it is finally stabilized (Fig. 2c). High-resolution TEM (HRTEM) imaging (Fig. 2d and Supplementary Fig. 5) and EDS characterization (Fig. 2e and Supplementary Fig. 6) of the entire particle confirm the single-crystal structure and homogeneous distribution of metal elements within the resulting HEA-NPs. Therefore, the dynamic evolution of the HEA-NPs formation can be summarized as mixing assisted by a hydrogen gas bubble, followed by isothermal solidification of the liquid alloy and reshaping during final crystallization.

Figure 2c shows that the isothermal solidification of the liquid alloy takes several seconds, which is contradictory to the common notion that the supercooled liquid alloy would undergo fast solidification[26]. To explore this further, we conduct atomic-resolution observation of the dynamic isothermal solidification (Supplementary Video 2). As shown in Fig. 3, we find oscillatory solidification of the liquid alloy. The H_2-gas-driven dynamics result in continuous splitting and reforming of the metal alloy domains. For instance (Fig. 3a), domain 2 with an initial crystalline structure converts to an amorphous liquid-like structure after it rapidly merges with domain 1. During the progression, crystallization occurs repeatedly, and then it breaks down into an amorphous structure on interaction with new domains. The oscillatory nucleation and disruption are shown (Fig. 3b,c) by tracking the crystal centre position and measuring the projected area of the crystalline domains with time. Notably, phase transitions between crystalline and amorphous states may occur within a single observation frame (0.1 s) (Fig. 3c). This implies that the solidification is fast, which helps effectively trap the high-entropy state of liquid metal.

Theoretical analysis of nucleation and solidification in this scenario supports our observation. According to classical nucleation theory[27], nucleation rate first increases with degree of supercooling, but eventually begins to decrease because of the retarding effect of a low absolute temperature on the rate of appearance of critically sized nuclei. This trend is captured by equation (1), in which ΔT is the degree of supercooling, T is the absolute temperature, ΔS_V is the difference in entropy

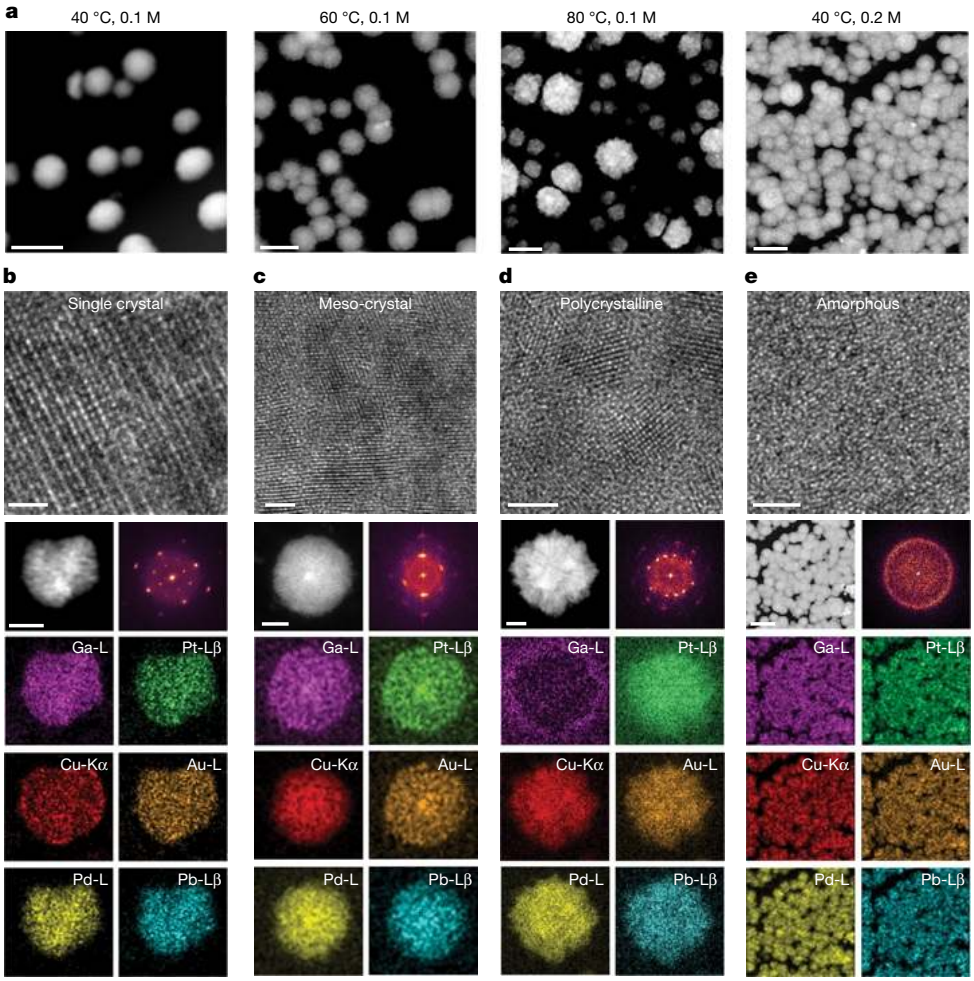

Fig. 4 | The controlled synthesis of HEA-NPs with various crystallinity and morphology. a, STEM images of synthesized HEA-NPs (GaPtPdPbAuCu) obtained at different temperatures and concentrations of metal ion precursors: 40 °C, 0.1 M; 60 °C, 0.1 M; 80 °C, 0.1 M; and 40 °C, 0.2 M. **b**–**e**, HRTEM images, along with corresponding FFT patterns and STEM–EDS mappings, show representative HEA-NPs synthesized under the following conditions: 40 °C with 0.1 M metal salt concentration (**b**), 60 °C with 0.1 M metal salt concentration (**c**), 80 °C with 0.1 M metal salt concentration (**d**) and 40 °C with 0.2 M metal salt concentration (**e**). Scale bars, 200 nm (**a**,**e**, bottom); 1 nm (**b**, top), 20 nm (**b**, bottom); 2 nm (**c**, top, **d**, top, **e**, top); 50 nm (**c**, bottom, **d**, bottom).

between the solid and liquid phases, γ is the interfacial energy between the solid and liquid phases and K is a geometrical prefactor. As our experiments take place at low temperatures, we speculate that the isothermal solidification process may occur in this regime with extreme supercooling and a suppressed nucleation rate resulting from a delay in the solidification process:

$$J = K\exp\left[\frac{-16\pi\gamma^3}{3k_BT\Delta S_V^2(\Delta T)^2}\right] \quad (1)$$

We also propose that when solid nuclei do appear, their growth is inhibited by the mixing motion introduced by hydrogen bubbles produced from the reduction of H^+, which destroys the nuclei and further delays solidification. This is consistent with our in situ observation that the hydrogen-gas-assisted stirring of the liquid repeatedly disrupts the crystallization. Finally, we note that at the beginning of the synthesis process, no Ga is present in the aqueous phase, and as a result, there exists a favourable thermodynamic driving force for the dissolution of Ga. The Ga dissolution, in combination with the metal ion reduction reactions at the interfaces, followed by the quick incorporation of foreign metal atoms into the Ga liquid metal alloy, drives the rapid composition changes leading to kinetically trapped high-entropy states during the isothermal solidification process.

Crystallinity and morphology control

Using the isothermal solidification strategy, we adjusted the reaction temperature and metal salt concentration to control the solidification rates. This allowed us to precisely regulate the morphology and crystallinity of the resulting HEAs (Fig. 4, Supplementary Figs. 7 and 8 and Supplementary Tables 2 and 3). The study specifically targets a system consisting of thermodynamically immiscible elements[7,28]: Ga, Pt, Pd, Au, Cu and Pb (Supplementary Table 4). Owing to the differences in atomic size, electronegativity and lattice parameters among these metals, phase separation often occurs during thermodynamic processing (Extended Data Fig. 3 and Supplementary Table 5), which makes this alloy an ideal candidate for exploring synthesis under non-equilibrium conditions.

At 40 °C, metal atoms, produced through a gentle reaction, dissolved into the liquid Ga and were mixed thoroughly. As the melting point of the liquid alloy (which varies with its elemental composition) rises above 40 °C, the alloy solidified from a supercooled state, forming a uniform solid solution with high crystallinity (Fig. 4a,b and Supplementary Fig. 9). For small particles (size below 100 nm), we use HRTEM images of entire particles and FFT analysis to confirm their single-crystal structure (Supplementary Fig. 10). For large particles, we use selected area electron diffraction (SAED) patterns to verify their single-crystal nature (Supplementary Fig. 8). However, not all

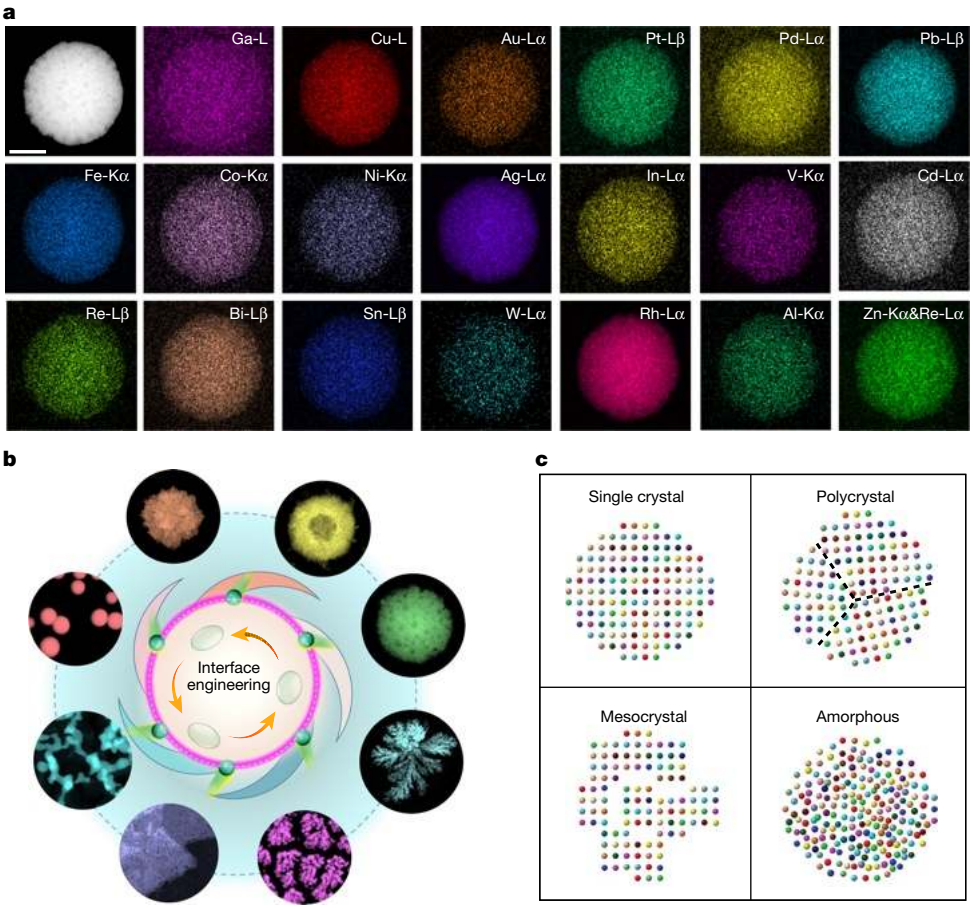

Fig. 5 | The isothermal solidification method is efficacious for synthesizing HEA nanomaterials with controlled composition, morphology and crystallinity. a, STEM–EDS elemental maps show HEAs can incorporate as many as 20 metal elements. **b**, HEAs with diverse shapes and morphologies can be obtained through liquid interface reactions. **c**, Schematic of the controllable crystallinity (single crystal, mesocrystalline, polycrystalline and amorphous structures) of synthesized HEA nanomaterials. Scale bar, 100 nm (**a**).

particles are perfect single crystals—some exhibit lattice defects. For example, the HRTEM image (Supplementary Fig. 11) shows various defects within a HEA particle, including lattice mismatch, lattice distortion and local structural disorder. These defects may result from factors such as atomic radius variations and lattice differences among different metal elements[29]. At higher temperatures (for example, 60 °C), the solidification rate increased, and the time required to achieve perfect crystallization is not sufficient. Consequently, the nanoparticles exhibit a mesocrystalline structure with a distinctive architecture (Fig. 4c, Extended Data Fig. 4 and Supplementary Fig. 12): large porous spherical particles (100–300 nm) composed of numerous smaller nanoclusters (2–5 nm). In general, the solidification of liquid alloys often results in volume shrinkage, which can contribute to the formation of a porous structure[30]. Moreover, the higher rate of gas generation can cause gas to become trapped within the alloy, further promoting the porosity[29]. Notably, within this mesocrystalline matrix, we observe local lattice distortions and bending (Extended Data Fig. 4), probably because of the stress induced by gas generation and the high surface tension of the liquid metal before solidification. By further increasing the temperature to 80 °C, polycrystalline HEA-NPs with a flower-like morphology are produced (Fig. 4d and Supplementary Fig. 13). EDS mapping shows that nearly all the Ga is consumed, leaving the remaining five elements evenly distributed throughout the particles. The complete consumption of Ga may stem from an accelerated solidification rate[31]. The polycrystalline phase and flower-like morphology may arise from dynamic heterogeneities and the mobility asymmetry of supercooled liquids[29]. The observed crystallinity variations with temperature are consistent with our theoretical predictions (Supplementary Fig. 14).

Amorphous HEAs are achieved by doubling the concentration of metal precursor solution at 40 °C while keeping all other parameters constant (Fig. 4e and Supplementary Figs. 15 and 16). This adjustment boosts the influx of foreign metals at the liquid–liquid interface by preserving their diffusion rate. Consequently, foreign atoms enter the liquid metal and accumulate rapidly, thus promoting solidification. In this case, we get spherical HEA-NPs with an amorphous phase. The solid spherical shape indicates that no gas entered the particle during the reaction at 40 °C, similar to the case in Fig. 4b. The uniform distribution of metal elements demonstrates that the metal atoms have diffused sufficiently, resulting in thorough mixing. Hence, we deduce that the amorphous structure arises from the swift dissolution of foreign metal atoms, leading to deep undercooling of the liquid alloy, followed by the prompt solidification of the liquid alloy. As foreign atoms enter, the melting point of the liquid alloy quickly surpasses its temperature. Nevertheless, without crystal nucleation, the liquid metal maintains its supercooled state to maintain its liquid form. Once solidification is triggered, it proceeds rapidly, leading to an amorphous solid.

The precise control over the crystallinity of these HEAs confirms the presence of distinct supercooled states and the varied solidification rates during isothermal solidification synthesis. In contrast to the rapid cooling solidification synthesis methods[1–3], the isothermal solidification provides the opportunity to control the crystallinity and morphology of HEAs (Supplementary Table 6). Notably, we have

achieved precise control over the crystallinity of HEAs, successfully synthesizing mesocrystalline HEAs (Extended Data Figs. 4 and 5).

Diversified synthesis of HEAs

The isothermal solidification strategy demonstrates its robust abilities for controlled synthesis of a diverse array of HEA nanomaterials, beyond the HEA-NPs. In terms of composition control, a broad range of metallic elements can be incorporated into the liquid Ga metal, successfully forming quinary, senary, septenary, octonary, nonary, decennary and even undecennary HEAs (Fig. 4, Extended Data Figs. 6 and 7 and Supplementary Figs. 17–21). Moreover, Ga can be completely consumed to produce Ga-free HEAs (Fig. 4d, Extended Data Fig. 6 and Supplementary Figs. 22 and 23). As shown in Fig. 5a, we have synthesized HEAs with more than 20 distinct elements, each possessing unique crystal structures, melting points and atomic radii. This ability highlights the versatility in generating a broad spectrum of HEA-NPs with diverse elemental combinations (Fig. 5a and Supplementary Table 7). HRTEM and EDS confirm the compositional homogeneity of these nanoparticles, showing no phase or elemental segregation (Extended Data Fig. 8 and Supplementary Figs. 24 and 25).

Apart from the mixing of diverse elements, the morphology and crystallinity of these HEAs can also be tuned, similar to the HEA-NPs in Fig. 4. By adjusting the reaction kinetics at liquid–liquid interfaces, we can synthesize a spectrum of structures spanning from zero to three dimensions, including solid, porous, hollow spheres, nanoflowers, nano dendrites, two-dimensional porous nanosheets, as well as three-dimensional networks and hierarchical structures (Fig. 5b, Extended Data Figs. 6, 7, 9 and 10 and Supplementary Figs. 26 and 27).

HEA-NPs with zero-dimension morphology (including solid, porous and flower-like nanoparticles) are typically obtained by using spherical liquid metal precursors (as opposed to flakes of Ga) (Methods and Extended Data Fig. 10). At 30 °C (Extended Data Fig. 10a), when liquid Ga metal is used as precursor (red outline), the resulting HEA-NPs tend to form phase-separated structures resembling egg-yolk and core-shell configurations. By increasing the temperature to 40 °C, HEA-NPs with solid sphere shapes can be achieved (red outline) in Extended Data Fig. 10b. Further increasing the temperature to 60 °C and 80 °C, HEA-NPs with porous spherical, flower-like, dendritic and snowflake-like morphologies can be obtained (Fig. 4c,d and Extended Data Fig. 10d,f). This implies that raising the reaction temperature may enhance the uniform distribution of elements, the formation of porous structures and a more diversified morphology in HEAs. By controlling the size of the liquid metal precursor, we can tune the sizes of the resulting high-entropy nanomaterials (Supplementary Fig. 28). This approach enables the synthesis of high-entropy nanomaterials with a range of sizes (Supplementary Fig. 29). Moreover, further investigations have demonstrated that, under identical reaction conditions, variations in precursor size do not affect elemental distribution or HEA formation (Supplementary Fig. 30).

By using liquid Ga alloy instead of pure Ga precursor, we can obtain HEA-NPs with porous structure at 40 °C and even room temperature (about 25 °C) (Extended Data Fig. 10a,b, yellow outline). Using a liquid alloy precursor with a lower melting point yields similar effects as increasing the reaction temperature. This may be attributed to the fact that the lower melting point of the liquid Ga alloy further promotes the reduction reaction at the interfaces and the mixing of the foreign metal atoms. At the elevated temperatures (for example, 60 °C or above), the impact of the liquid metal precursor is not notably pronounced, and both liquid Ga and liquid Ga-based alloys can yield porous or more diversified structures (Fig. 4c,d and Extended Data Fig. 10d,f).

Without the addition of HCl to the metal salt solution, the formation of HEAs at low temperatures (for example, 30 °C and 40 °C) is hindered, as the oxide on the surface of the liquid metal acts as a passivation layer blocking the interface reaction. However, increasing the temperature can resolve this issue, allowing for the formation of HEAs with various morphologies (Extended Data Fig. 10c,e). We further find that ellipsoidal HEA-NPs are generated when spherical liquid metal precursors are used (Extended Data Fig. 10c, indigo outline), HEAs with irregular shapes are obtained as irregular metal precursors are used (Extended Data Fig. 10c, green outline), and two-dimensional film metal precursors are used to synthesize two-dimensional nanosheets, three-dimensional networks, three-dimensional hierarchical structures and some other intricate structures (Extended Data Fig. 10c,e, white outline). Accompanying the morphological changes, the crystallinity can also be modified, enabling the synthesis of HEAs with single-crystalline, mesocrystalline, polycrystalline and amorphous structures depending on the rate of isothermal solidification (Figs. 4 and 5c and Extended Data Figs. 5–7).

Conclusion

We demonstrate an isothermal solidification strategy for the synthesis of HEAs with controlled crystallinity, morphology and composition at low temperatures. By directing the metal ion reduction reactions to the liquid–liquid interfaces, the foreign metal mixing rate is substantially enhanced. The fast metal mixing combined with the rapid Ga consumption effectively induces liquid alloys with a high concentration of solute metal above the thermodynamic solubility limitation at low temperatures. The gas-bubble-enhanced mixing and fluctuations of crystallization during isothermal solidification highlight an unexplored pathway to kinetically trap the high entropy state. This strategy broadens the scope of HEA synthesis and discovery, allowing the creation of previously unattainable HEAs with diverse structural configurations. The liquid–liquid interface reaction enables unhindered solidification, resulting in intricate solidification patterns at room temperature with promising applications, such as three-dimensional printing of metals, catalysis and batteries. Further exploration of the diverse HEAs has the potential to expand their applications across broader fields, spanning material science, chemistry and biomedicine.

Online content

Any methods, additional references, Nature Portfolio reporting summaries, source data, extended data, supplementary information, acknowledgements, peer review information; details of author contributions and competing interests; and statements of data and code availability are available at https://doi.org/10.1038/s41586-025-09530-w.

1. Yao, Y. et al. Carbothermal shock synthesis of high-entropy-alloy nanoparticles. *Science* **359**, 1489–1494 (2018).
2. Li, M. et al. High-entropy alloy electrocatalysts go to (sub-) nanoscale. *Sci. Adv.* **10**, eadn2877 (2024).
3. Gao, S. et al. Synthesis of high-entropy alloy nanoparticles on supports by the fast moving bed pyrolysis. *Nat. Commun.* **11**, 2016 (2020).
4. Wang, B. et al. General synthesis of high-entropy alloy and ceramic nanoparticles in nanoseconds. *Nat. Synth.* **1**, 138–146 (2022).
5. Chen, P.-C. et al. Polyelemental nanoparticle libraries. *Science* **352**, 1565–1569 (2016).
6. Sun, Y. & Dai, S. High-entropy materials for catalysis: a new frontier. *Sci. Adv.* **7**, eabg1600 (2021).
7. Yao, Y. et al. High-entropy nanoparticles: synthesis-structure-property relationships and data-driven discovery. *Science* **376**, eabn3103 (2022).
8. Xin, Y. et al. High-entropy alloys as a platform for catalysis: progress, challenges, and opportunities. *ACS Catal.* **10**, 11280–11306 (2020).
9. Liu, Y.-H. et al. Toward controllable and predictable synthesis of high-entropy alloy nanocrystals. *Sci. Adv.* **9**, eadf9931 (2023).
10. Ouyang, B. & Zeng, Y. The rise of high-entropy battery materials. *Nat. Commun.* **15**, 973 (2024).
11. Liu, D. et al. Exceptional fracture toughness of CrCoNi-based medium-and high-entropy alloys at 20 kelvin. *Science* **378**, 978–983 (2022).
12. Cao, G. et al. Liquid metal for high-entropy alloy nanoparticles synthesis. *Nature* **619**, 73–77 (2023).
13. Kang, Y. et al. Mesoporous multimetallic nanospheres with exposed highly entropic alloy sites. *Nat. Commun.* **14**, 4182 (2023).

14. Zhan, C. et al. Subnanometer high-entropy alloy nanowires enable remarkable hydrogen oxidation catalysis. *Nat. Commun.* **12**, 6261 (2021).
15. Li, Y. et al. Cu-based high-entropy two-dimensional oxide as stable and active photothermal catalyst. *Nat. Commun.* **14**, 3171 (2023).
16. Zavabeti, A. et al. A liquid metal reaction environment for the room-temperature synthesis of atomically thin metal oxides. *Science* **358**, 332–335 (2017).
17. Idrus-Saidi, S. A. et al. Liquid metal synthesis solvents for metallic crystals. *Science* **378**, 1118–1124 (2022).
18. Taccardi, N. et al. Gallium-rich Pd–Ga phases as supported liquid metal catalysts. *Nat. Chem.* **9**, 862–867 (2017).
19. Hong, S.-J. & Suryanarayana, C. Mechanism of low-temperature θ-$CuGa_2$ phase formation in Cu-Ga alloys by mechanical alloying. *J. Appl. Phys.* **96**, 6120–6126 (2004).
20. Brandes, E. A. & Brook, G. *Smithells Metals Reference Book* (Elsevier, 2013).
21. Dean, J. A. *Lange's Handbook of Chemistry* (McGraw-Hill, Inc., 1999).
22. Yao, Y. et al. Computationally aided, entropy-driven synthesis of highly efficient and durable multi-elemental alloy catalysts. *Sci. Adv.* **6**, eaaz0510 (2020).
23. Chang, X., Zeng, M., Liu, K. & Fu, L. Phase engineering of high-entropy alloys. *Adv. Mater.* **32**, 1907226 (2020).
24. Young, D. A. *Phase Diagrams of the Elements* (Univ. California Press, 2023).
25. Gan, T., Handschuh-Wang, S., Shang, W. & Zhou, X. GaOOH crystallite growth on liquid metal microdroplets in water: influence of the local environment. *Langmuir* **38**, 14475–14484 (2022).
26. Turnbull, D. Kinetics of solidification of supercooled liquid mercury droplets. *J. Chem. Phys.* **20**, 411–424 (1952).
27. Kalikmanov, V. I. *Nucleation Theory* (Springer, 2013).
28. Takeuchi, A. & Inoue, A. Classification of bulk metallic glasses by atomic size difference, heat of mixing and period of constituent elements and its application to characterization of the main alloying element. *Mater. Trans.* **46**, 2817–2829 (2005).
29. Tandoc, C., Hu, Y.-J., Qi, L. & Liaw, P. K. Mining of lattice distortion, strength, and intrinsic ductility of refractory high entropy alloys. *npj Comput. Mater.* **9**, 53 (2023).
30. Khalajzadeh, V. & Beckermann, C. Simulation of shrinkage porosity formation during alloy solidification. *Metall. Mater. Trans. A* **51**, 2239–2254 (2020).
31. Gránásy, L., Pusztai, T., Börzsönyi, T., Warren, J. A. & Douglas, J. F. A general mechanism of polycrystalline growth. *Nat. Mater.* **3**, 645–650 (2004).

Methods

Chemicals

All chemicals used in this study were commercially available, and no further purification was required. These include gallium (Ga; 99.99%), indium (In; 99.99%), tin (Sn; 99.999%), zinc (Zn; 99.8%), aluminium (Al; 99%), vanadium(III) chloride (VCl_3; 97%), cadmium chloride ($CdCl_2$; 99.99%), iron(III) chloride hexahydrate ($FeCl_3{\cdot}6H_2O$; 98.0–102%), cobalt(II) chloride hexahydrate ($CoCl_2{\cdot}6H_2O$; 98%), nickel(II) chloride hexahydrate ($NiCl_3{\cdot}6H_2O$; 99.9%), copper(II) chloride dihydrate ($CuCl_2{\cdot}2H_2O$; 99.0%), zinc chloride ($ZnCl_2$; 98%), lead(II) chloride ($PbCl_2$; 99.999%), palladium(II) chloride ($PdCl_2$; 99%), platinum(II) chloride ($PtCl_2$; 99%), rhodium(II) chloride hydrate ($RhCl_3{\cdot}xH_2O$; 38–40%), bismuth(III) chloride ($BiCl_3$; 99.99%), tungsten(VI) chloride (WCl_6; 99.9%), gold(III) chloride hydrate ($HAuCl_4{\cdot}xH_2O$; about 50% Au basis), silver nitrate ($AgNO_3$; 99.0%), 1-dodecanethiol (98%), 2-propanol (99.5%), acetone (CH_3COCH_3; 99.9%) and hydrochloric acid (HCl; 37%) were purchased from Sigma-Aldrich. Rhenium(III) chloride ($ReCl_3$; 61.4–65.9% Re) was purchased from Thermo Scientific Chemicals. To prepare the solutions, an ultrapure purification system (Milli-Q Advantage A10) was used, which produced deionized water with a resistance of 18.2 MΩ cm.

Preparation of Ga and Ga alloy nanoparticle precursors

We used two methods for the synthesis of Ga NPs. The first approach involves the synthesis of Ga NPs using a previously reported sonication technique[32]. Specifically, a mixture of Ga (100 mg, 1.43 mmol), 1-dodecanethiol (289 mg, 1.43 mmol) and 2-propanol (10 ml) was placed in a vial and subjected to sonication for 2 h. Then, the obtained NPs were separated by centrifugation and washed three times with acetone to remove the remaining 1-dodecanethiol. Finally, the Ga NPs were redispersed in acetone for storage.

The second method involves scratching about 0.02 mg liquid Ga metal onto a carbon film substrate to form irregular thin film flakes (Supplementary Fig. 31a). These thin film flakes were remarkably stable because of the formation of oxide layers on the Ga surface. Subsequently, immersing the substrate coated with the Ga/Ga-oxide flakes in a 0.1 M HCl aqueous solution for 3 s triggered a reaction with the oxide layer, transforming the irregular Ga/Ga-oxide thin film flakes into Ga metal nanoparticles (Supplementary Fig. 31b).

Galinstan was prepared by mixing Ga, In and Sn metals at 250 °C until complete melting. The weight ratio of Ga:In:Sn was 68.5:21.5:10.0. GISZ alloys were prepared by mixing Ga, In, Sn and Zn metals with various compositions in quartz tubes under a vacuum of approximately 5×10^{-4} Pa and heated at 250 °C for several hours until complete melting in a thermostatic oil bath[33]. After melting, the alloys were cooled to room temperature and transferred into sealed vials using a plastic transfer pipette for further use. We used the same scratching method to prepare Galinstan and GISZ nanoparticles with different film flakes. Furthermore, we immersed the Ga-based alloy-loaded substrate in a 0.1 M HCl aqueous solution for 3 s to get Galinstan and GISZ nanoparticles. After all nanoparticle formation, we gently placed the sample into deionized water to remove the chloride for further use.

Preparation of Ga–Cu and Cu–Pd binary alloys

First, a commercial Au TEM grid coated with a carbon film was used as the substrate. A thin layer of liquid Ga metal (approximately 0.02 mg) was applied to the carbon film side by gentle scratching. Subsequently, we immersed the Ga-loaded TEM grid in a 0.1 M HCl aqueous solution for 3 s. The HCl removed the native oxide layer on the Ga surface, allowing the liquid Ga to spontaneously break into numerous nanoparticles because of surface tension. The Au grid, now loaded with Ga nanoparticles, was thoroughly rinsed with deionized water to remove residual chloride ions and then dried. It was then placed on an IKA RCT magnetic hotplate, heated and maintained at a constant temperature of 60 °C. A drop of $CuCl_2$ aqueous solution was added and allowed to react for 2 min. The resulting sample was washed again with deionized water, yielding Ga–Cu binary alloy particles as shown in Fig. 1d. By substituting the copper salt solution with an Au or Pa salt solution, binary Ga–Au and Ga–Pd alloys can also be synthesized (Supplementary Figs. 32 and 33).

For the synthesis of Cu–Pd binary alloy nanoparticles (Fig. 1e), Ga particles were heated and maintained at 80 °C. An aqueous solution of $PdCl_2$ was used in place of $CuCl_2$. All other experimental conditions and procedures were identical to those used for the synthesis of the Ga–Cu alloy.

Preparation of single-crystal GaCuPdPtAuPb HEA-NPs

To synthesize GaCuPdPtAuPb HEA-NPs, a nickel TEM grid coated with a carbon film was used as the substrate to eliminate any potential elemental interference from the grid during alloy formation. Ga nanoparticles were prepared using the second method (scratching method) to load on the substrate. The Ga particles were then heated and maintained at 60 °C on an IKA RCT magnetic hotplate. Subsequently, 0.1 M mixing aqueous solutions (30 µl) of $CuCl_2$, $PbCl_2$, $PdCl_2$, $PtCl_2$ and $HAuCl_4$ were dropped onto the carbon film and allowed to react for two minutes. The resulting sample was rinsed thoroughly with deionized water to obtain the single-crystalline HEA-NPs shown in Fig. 1f.

Preparation of GaCuPdPtAuPb HEA with tunable morphologies and structures

To prepare GaCuPdPtAuPb HEA with adjustable morphology and structure, we also used the scratching method to form Ga nanoparticle precursor on a nickel TEM grid coated with a carbon film. The TEM grid loaded with Ga nanoparticles was heated to 40 °C, after which a 0.1 M mixed aqueous solution (30 µl) containing HCl, $CuCl_2$, $PbCl_2$, $PdCl_2$, $PtCl_2$ and $HAuCl_4$ was dropped onto the carbon film and allowed to react for 2 min. The resulting sample was thoroughly rinsed with deionized water to yield the single-crystalline HEA-NPs shown in Fig. 4b. While keeping the reaction steps and conditions unchanged, we adjusted only the heating temperature of the TEM grid to 60 °C and 80 °C. This led to the formation of GaCuPdPtAuPb HEA-NPs with a mesocrystalline structure at 60 °C (Fig. 4c), and CuPdPtAuPb HEA-NPs with a polycrystalline structure at 80 °C (Fig. 4d). If the other reaction conditions are kept constant and the salt concentration is doubled relative to the conditions in Fig. 4b, an amorphous GaCuPdPtAuPb alloy can be obtained (Fig. 4e).

Preparation of HEA nanomaterials

To prepare the other HEA-NPs, we heated carbon-supported TEM grids containing Ga, Galinstan and GISZ alloy NPs on an IKA RCT magnetic hotplate stirrer at room temperature, 40 °C, 60 °C or 80 °C for 2 min. It should be noted that we selected various TEM carbon film grids depending on the synthesis of different HEAs to better assess the influence of the TEM grid on experimental outcomes. Then, we added a drop of a mixture of various metal salt solutions (0.1 M for each salt) to the grid, with or without 0.1 M HCl. After 1 min of reaction, we removed the remaining liquid and washed away the residual salt with deionized water. Then, the sample was loaded into a TEM for characterization.

For preparing HEA nanomaterials with different shapes, we used the scratching method to load Ga-based liquid metal onto a carbon substrate, creating various irregular thin films. The oxide layer forms spontaneously on the liquid metal surface, stabilizing the irregular film shape. Next, we applied salt solutions containing various metal cations (0.1 M for each salt) onto the substrate to react with the Ga-based liquid metal at different temperatures (25–80 °C) for 2 min, generating various non-granular HEAs. To prepare HEAs with more elements, Al was introduced to the Galinstan or GISZ alloys before adding salt solutions.

Material characterizations

The TEM characterizations were conducted using an image-corrected FEI ThemIS microscope operating at 60–300 kV. The microscope is

equipped for fast EDS mapping and S/TEM imaging. All TEM and HRTEM images were captured using an FEI Ceta2 camera. For EDS spectra and mapping, an FEI EDS detector with four windowless SDDs was used. It provides a solid angle of 0.7 steradians and 140 eV energy resolution, enabling elemental mapping with a high signal-to-noise ratio. During the TEM characterization process, we selected different TEM grids, washers and clips based on the element combinations of the HEA nanomaterials.

In situ liquid cell experiment for HEA-NPs formation

To study the alloying mechanisms of liquid metal with foreign metal source in the liquid phase environment, carbon film liquid cells were used in this experiment. First, we deposited the liquid GISZ alloy onto a carbon-supported gold grid by the scratching method. Next, the grid was swiftly immersed in a 0.1 M HCl solution for 1 s, followed by rinsing with deionized water, effectively forming GISZ nanoparticles onto the carbon-supported grid. After drying, 100 nl of $CuCl_2{\cdot}2H_2O$ aqueous solution (0.1 M) and 10 nl of 0.1 M HCl solution were dropped onto the GISZ-loaded carbon film. We covered the wet grid with another grid. After the liquid cell was assembled, it was loaded into the microscope for imaging. An FEI ThemIS 60-300 STEM/TEM with Cs-corrector was used for in situ imaging, and a beam current density of about 100 $e^- nm^{-2} s^{-1}$ was used for the study.

Excluding the influence of electron beam effects

To rule out the influence of the electron beam on the conclusions drawn from the in situ experiments, we conducted three systematic control experiments: ex situ experiments without electron beam exposure, in situ experiments without heating and in situ experiments with the electron beam blocked.

The ex situ control experiment without electron beam exposure excluded the influence of the electron beam on the alloying process. For all ex situ processes of HEA alloying, we can reach the high-entropy state after the reaction with no electron beam involved (Figs. 1f and 4). Therefore, the formation of HEA-NPs observed under controlled electron beam conditions can reflect the actual situation of ex situ synthesis.

Under the same electron beam conditions, the in situ control experiment without heating showed no alloying phenomena (Supplementary Fig. 34), confirming that alloying does not occur in the absence of heating. Therefore, we know thermal heating triggers the alloying process.

Third, in our in situ experiment with thermal heating at 60 °C, we found particles outside the viewing field that were not exposed to the electron beam during the reaction could still form HEAs (Supplementary Fig. 35), which demonstrates that HEA formation is independent of the electron beam.

Therefore, based on these findings, we confirm that the formation of HEA in our in situ experiment is driven by thermal heating rather than the electron beam.

ICP-OES characterization. The as-synthesized HEA powders containing Ga, Pb, Pd, Pt, Cu and Au were dissolved using freshly prepared aqua regia (3:1 v/v HCl:HNO_3). After the acid was added to the powders, the suspension was subjected to sonication at room temperature for 15 min to promote initial dissolution. The mixture was then gently heated to 60 °C on a hotplate until complete visual dissolution of the solids was observed. Additional aqua regia was added dropwise as needed to ensure full digestion. Following digestion, the solution was cooled to room temperature, and a measured aliquot was diluted with 2% HNO_3 (v/v) before the ICP-OES analysis. All solutions were prepared using ultrapure water. The ICP-OES measurements were carried out using an Agilent 5800 Series VDV ICP-OES instrument. Axial viewing mode was selected for the detection of each element. An internal standard (yttrium) was used to correct for instrumental drift and matrix effects. Calibration accuracy and stability were verified using both an initial calibration verification standard and a continuing calibration verification standard. A reagent blank was also analysed to correct for background contamination.

XPS characterization

XPS analysis was performed on the six elements (GaCuPdPtAuPb) HEA-NPs (Supplementary Figs. 36 and 37). XPS analysis was conducted using a Thermo Scientific K-AlphaPlus instrument, equipped with a monochromatic Al Kα radiation source emitting at 1,486.7 eV. The measurement area was configured to an elliptical shape of 200 × 400 μm, and a flood gun was used for charge compensation. For spectral acquisition, the pass energy settings were 200 eV for survey spectra and 50 eV for high-resolution spectra, with an energy resolution maintained at 0.1 eV. The analysis chamber maintained the pressure of approximately 1×10^{-9} mbar during data acquisition. Data processing was executed using the Thermo Scientific Avantage XPS software, with peak fitting performed through a combination of Gaussian and Lorentzian shapes and a Shirley background subtraction. Reference for all peak positions was established using the C 1*s* peak from adventitious carbon at 284.4 eV. The XPS spectra covered several binding energy regions, including XPS Survey, Ga 3*d*, Cu 2*p*, C 1*s*, O 1*s*, Pt 4*f*, Au 4*f*, Pb 4*f* and Pd 3*d* orbitals, ensuring comprehensive surface composition analysis.

Data availability

All data generated or analysed during this study are available in the paper and its Supplementary Information.

32. Yamaguchi, A., Mashima, Y. & Iyoda, T. Reversible size control of liquid-metal nanoparticles under ultrasonication. *Angew. Chem. Int. Ed.* **54**, 12809–12813 (2015).
33. Yu, Q. et al. Identifying surface structural changes in a newly-developed Ga-based alloy with melting temperature below 10 °C. *Appl. Surf. Sci.* **492**, 143–149 (2019).

Acknowledgements This work was supported by the US Department of Energy, Office of Science, Office of Basic Energy Sciences (BES), Materials Sciences and Engineering Division under contract no. DE-AC02-05-CH11231 within the in situ TEM program (KC22ZH) and under contract no. DE-AC02-05-CH11231 within the D2S2 program (KCD2S2). Work at the Molecular Foundry of Lawrence Berkeley National Laboratory (LBNL) was supported by the US Department of Energy under contract no. DE-AC02-05CH11231. Y.H. acknowledges support from the National Science Foundation under award 2404462.

Author contributions Q. Zhang and H.Z. conceived this work. Q. Zhang designed and performed the in situ TEM experiments. Q. Zhang and Y.C. performed the ex situ experiment on HEA synthesis and HEA characterization. Y.L. performed electrocatalytic tests under the supervision of Y.H.; L.C. performed the XPS characterization and analysed the XPS data; M.C.G. discussed the thermodynamic and kinetic theory for the synthesis method under the supervision of K.A.P.; Q. Zhang, Z.S., Y.C., Q. Zheng, K.C.B., L.C. and H.Z. carried out data analysis. Q. Zhang and H.Z. co-wrote the paper with input from all authors. This work was done under the supervision of H.Z.

Competing interests The authors declare no competing interests.

Additional information
Supplementary information The online version contains supplementary material available at https://doi.org/10.1038/s41586-025-09530-w.

Correspondence and requests for materials should be addressed to Haimei Zheng.

Peer review information *Nature* thanks Yusuke Yamauchi and the other, anonymous, reviewer(s) for their contribution to the peer review of this work.

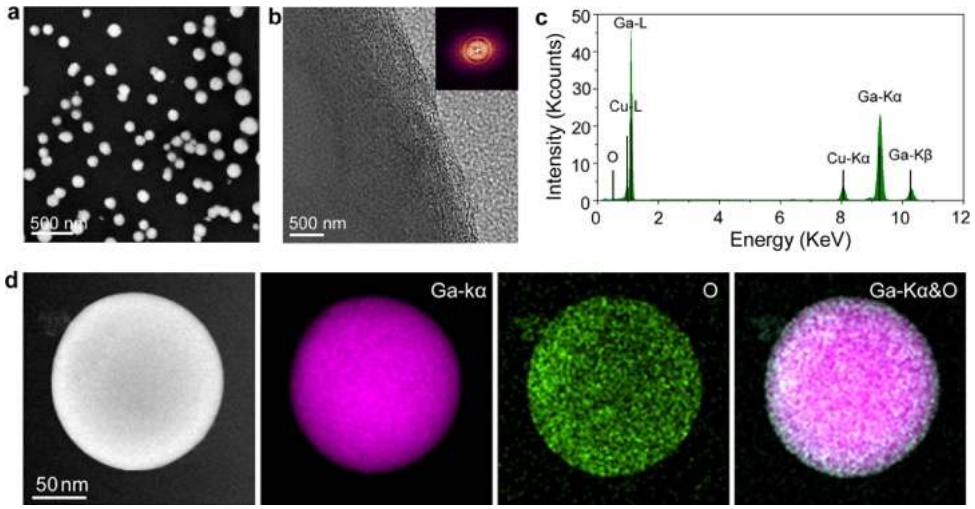

Extended Data Fig. 1 | TEM characterization of Ga nanoparticles. a, A low-magnification STEM image reveals the size characteristics of Ga nanoparticles. **b**, The HRTEM image, along with the corresponding FFT pattern of the Ga nanoparticle, indicates its amorphous structure. **c**, A STEM-EDS spectrum of a Ga nanoparticle confirms the presence of Ga and O elements, with Cu signals originating from the supporting Cu grid. **d**, STEM-EDS mapping of a Ga nanoparticle: HAADF image, Ga-Kα map, O map, and Ga-Kα&O map. The presence of O exclusively distributed on the shell part demonstrates the existence of an oxide shell.

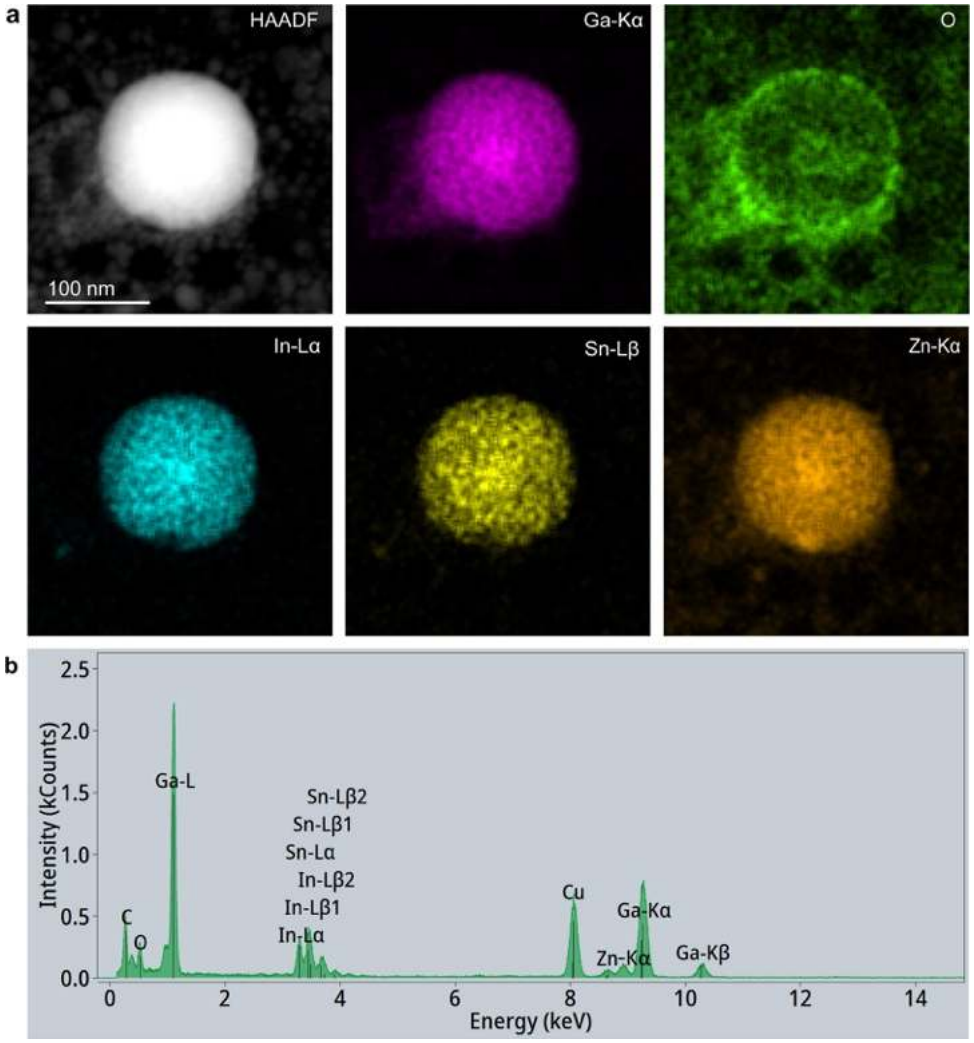

Extended Data Fig. 2 | EDS characterization of a GISZ nanoparticle. **a**, STEM-EDS mapping of a GISZ nanoparticle including HAADF image, Ga-Kα map, In-Lα map, Sn-Lβ map, Zn-Kα map, and O map. The presence of O exclusively distributed on the shell part demonstrates the existence of an oxide shell. **b**, The STEM-EDS spectrum of a GISZ nanoparticle confirms the presence of Ga, In, Sn, Zn, and O elements, with Cu signals attributed to the underlying Cu grid.

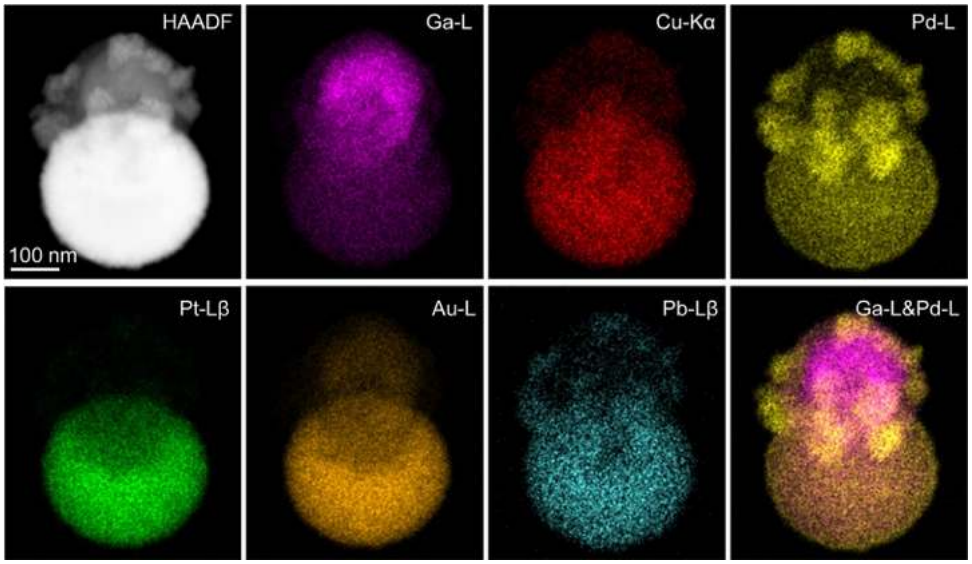

Extended Data Fig. 3 | TEM characterization of HEA with phase separation. STEM-EDS mapping of the heterostructured HEA-NP includes HAADF imaging along with elemental maps: Ga-L, Cu-Kα, Pd-L, Pt-Lβ, Au-L, Pb-Lβ, and a combined Ga-L & Pd-L map. The EDS mapping reveals a non-uniform elemental distribution within the nanoparticles, with the Ga-L & Pd-L maps highlighting the distinct phase segregation.

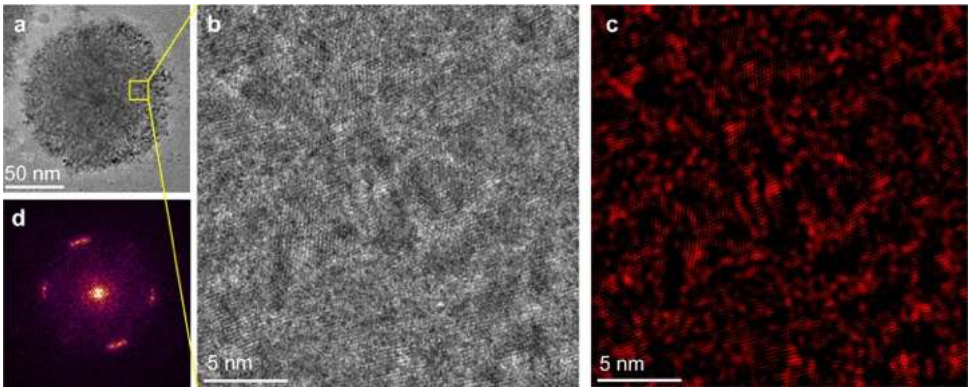

Extended Data Fig. 4 | TEM characterization of a mesocrystal HEA-NPs (corresponding to Fig. 4c). a, A low-magnification TEM image reveals a large, porous spherical particle composed of numerous smaller nanoclusters. **b**, An enlarged view of the mesocrystal structure. **c**, pseudo-color image of (b). **d**, The corresponding FFT pattern demonstrates that the crystalline domains are not perfectly aligned, indicating the lattice distortion.

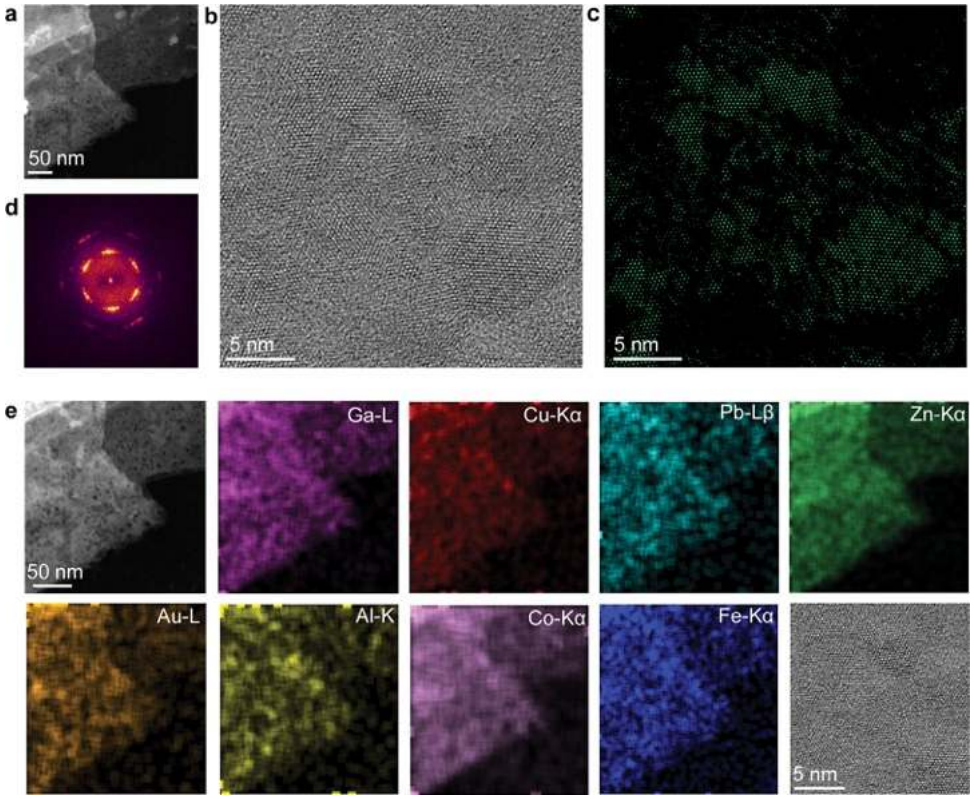

Extended Data Fig. 5 | Characterization of mesocrystal HEA nanosheets. **a**, A low-magnification STEM image highlights the two-dimensional morphology of the high-entropy nanosheets. **b**, The HRTEM image reveals their mesocrystal structure, with individual single crystalline domains exhibiting parallel crystallographic alignment while remaining spatially separated. **c**, An inverse fast Fourier transform (IFFT) image of the HRTEM emphasizes the distinct, separated crystal domains. **d**, The corresponding FFT pattern indicates that the crystalline domains are not perfectly aligned, showing signs of rotational misalignment. **e**, STEM-EDS maps demonstrate that the elements are uniformly distributed throughout the nanosheets.

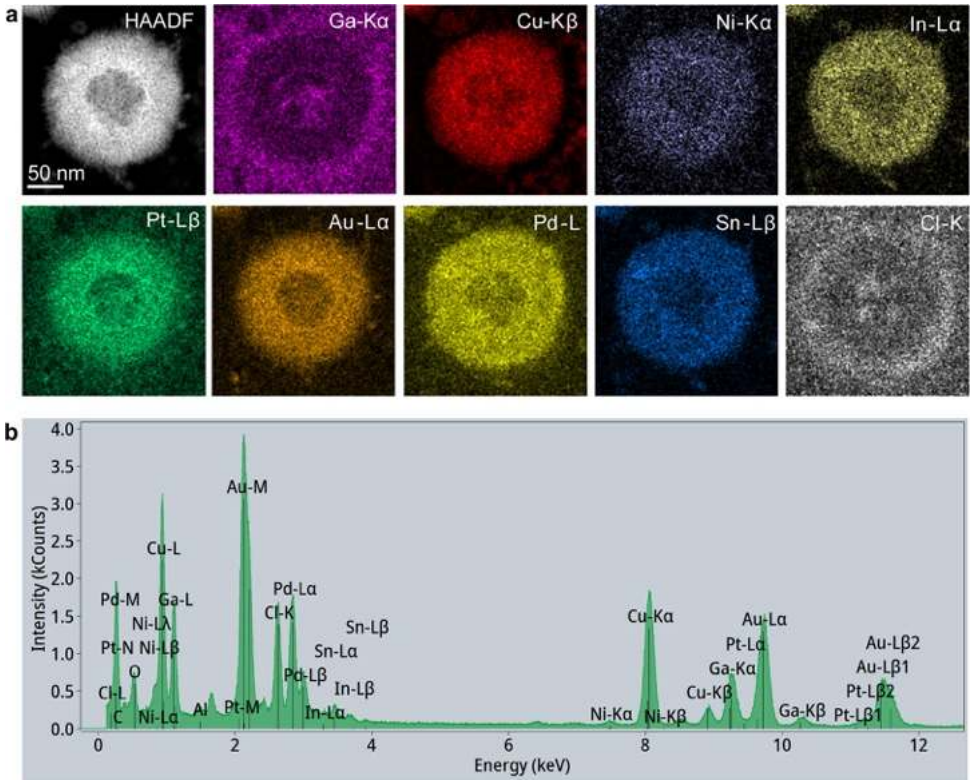

Extended Data Fig. 6 | EDS characterization of the HEA-NPs using Galinstan precursor at 40 °C. a, STEM-EDS mapping of the HEA-NPs: HAADF image, Ga-Kα map, Cu-Kβ map, Ni-Kα map, In-Lα map, Pt-Lβ map, Au-Lα map, Pd-L map, Sn-Lβ map, and Cl-K map. The EDS mapping reveals uniform elemental distribution within the nanoparticle. Cl does not belong to the HEA composition. **b**, The EDS spectrum of the HEA reveals the presence of C, O, Ga, Cu, Ni, In, Pt, Au, Pd, and Cl elements. C, O, and Cl originate from the carbon supporting film and residual salts.

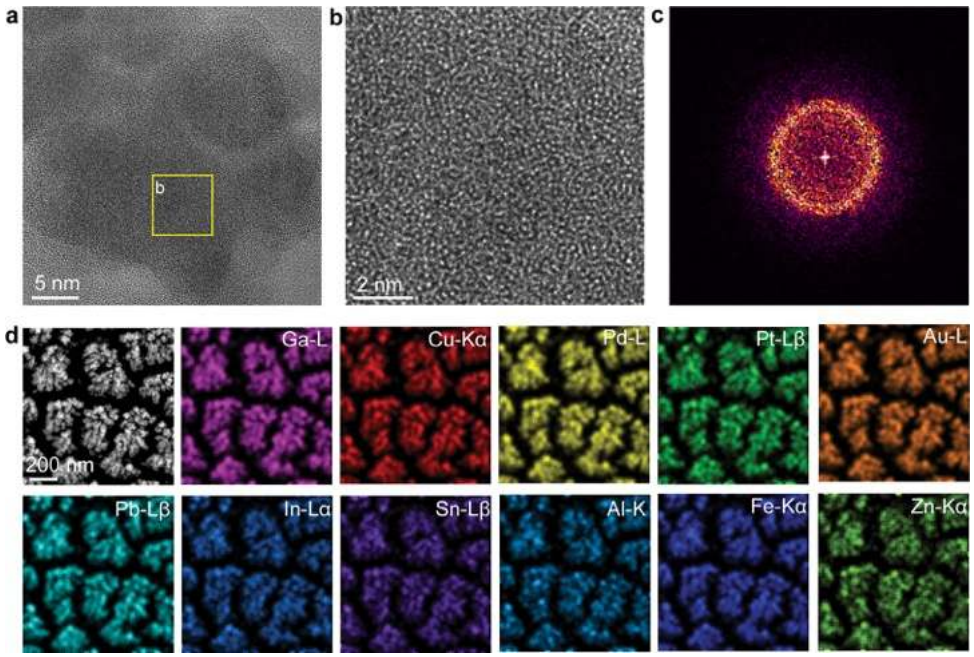

Extended Data Fig. 7 | Structural analysis of hierarchical HEA nanomaterials. a, TEM image of the basic flower structure. **b**, HRTEM showing the amorphous structure. **c**, the corresponding FFT (b). **d**, STEM-EDS maps of the three-dimensional hierarchical nanostructures show the elemental distribution.

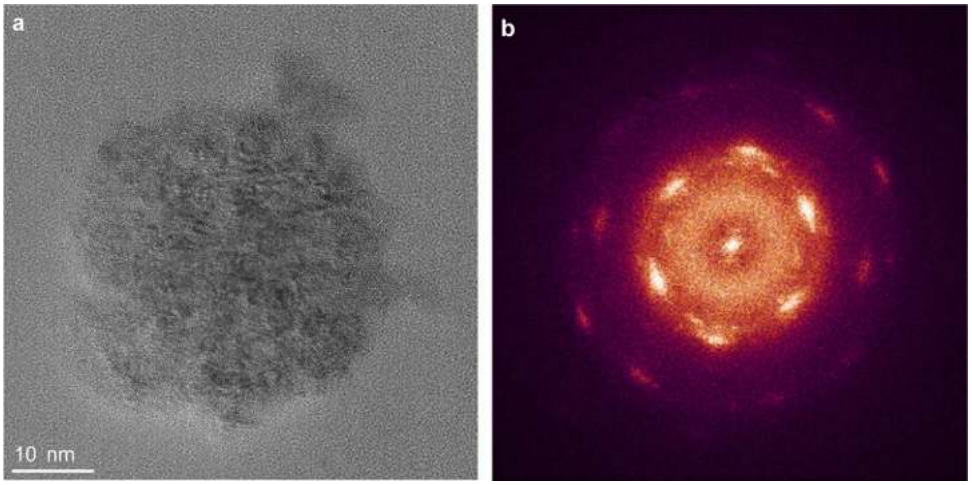

Extended Data Fig. 8 | TEM characterization of HEA with 20 elements (corresponding to Fig. 5a). a, HRTEM image reveals the crystal structure of the HEA-NPs. **b**, The corresponding FFT pattern reveals its mesocrystal structure.

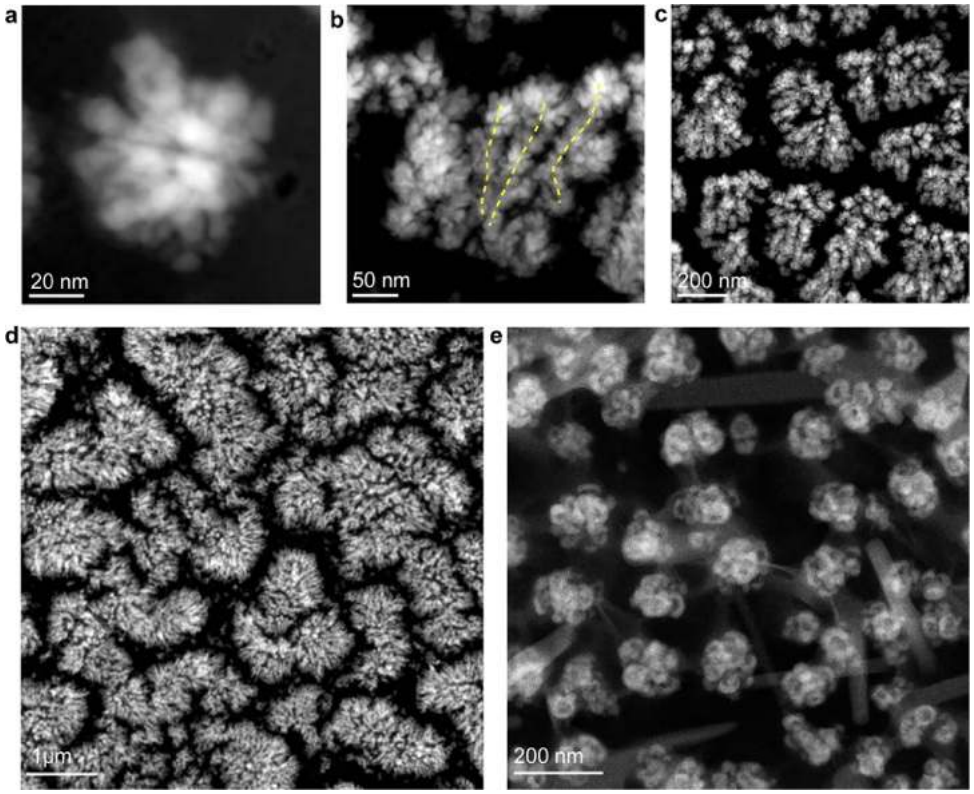

Extended Data Fig. 9 | Configurational analysis of selected three-dimensional hierarchical HEAs. a-**c**, STEM images of the three-dimensional HEA structure with "grape bunches" morphology. **a**, Flower structure of the basic building block. **b**, The flower structures are aligned to form a chain. Yellow dashed lines highlight the chain structure. **c**, Chain-like structures aggregate to form large grape-bunch-like assemblies. **d**, The three-dimensional HEA structure in the shape of feathers. **e**, The three-dimensional HEA structure with "plum blossoms" morphology.

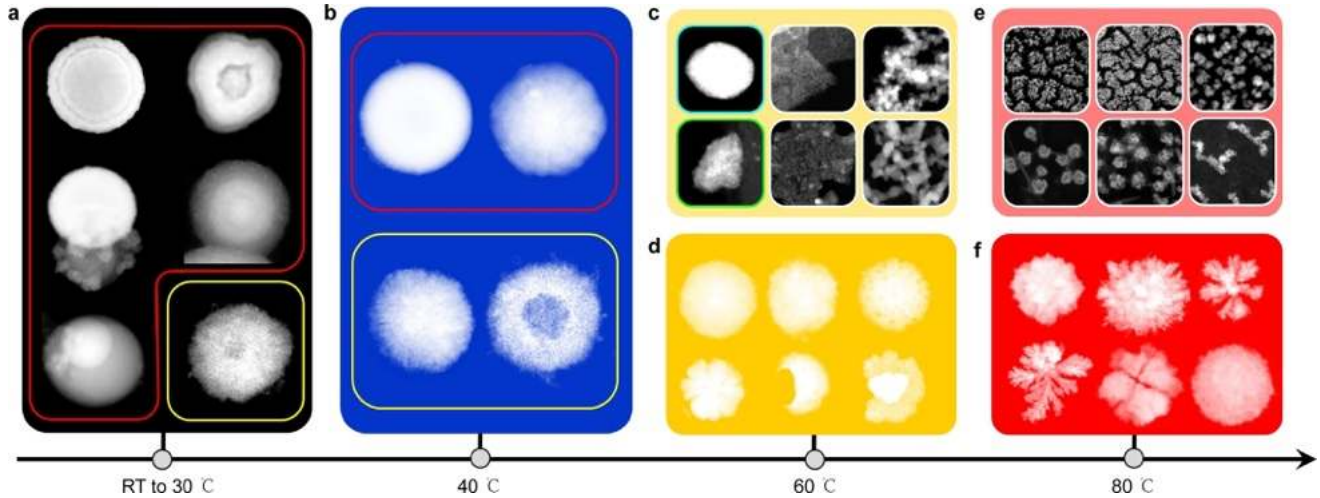

Extended Data Fig. 10 | Morphology diagram of HEA nanomaterials. STEM images show the diverse morphology of HEAs. **a**, To synthesize nanoparticles in panel (a), we utilize sphere liquid Ga (marked with red outline) or liquid Ga alloy (marked with yellow outline) as precursors. Additionally, we introduce HCl into the metal salt solution to eliminate the surface oxide of the Ga and Ga alloy particles. The reaction temperature with the red outline is 30 °C and the reaction temperature with yellow outline is room temperature. **b**, **d**, **f**, The synthesis conditions for the particles depicted in panel (b), (d), and (f) mirror those in panel (a), but with elevated reaction temperatures of 40 °C, 60 °C, and 80 °C. **c**, We employ spherical shape (marked with indigo outline), irregular shape (marked with green outline), and two-dimensional-film (marked with white outline) liquid Ga/Ga alloy precursors, without the addition of HCl in the metal salt solution, and the reaction temperature is 60 °C. **e**, For HEA synthesis, we use two-dimensional films of liquid Ga/Ga alloy precursors and the reaction temperature is 80 °C.